Enhancing two-photon spontaneous emission in rare earths using graphene and graphene nanoribbons

Colin Whisler, Gregory Holdman, D. D. Yavuz, and Victor W. Brar*
Department of Physics, University of Wisconsin–Madison, 1150 University Avenue, Madison, Wisconsin 53706, USA

(Received 2 January 2023; revised 24 March 2023; accepted 14 April 2023; published 10 May 2023)

The enhancement of two-photon spontaneous emission (2PSE) from trivalent and divalent rare earth ions in proximity to graphene and graphene nanoribbons is calculated for achievable experimental conditions using a combination of finite difference time domain simulations and direct computation of transition rates between energy levels in rare earths. For Er^{3+}, we find that the 2PSE rate is initially 8 orders lower than the single-photon spontaneous emission rate but that, with enhancement, 2PSE can reach 2.5% of the overall decay. When graphene nanoribbons are used, we also show that the emission of free-space photon pairs from Er^{3+} at 3–3.2 μm via 2PSE can be increased by ∼400. Our calculations show significantly less relative graphene-enhanced 2PSE than previous works, and we attribute this variation to differences in emitter size and assumed graphene mobility. We also show that the internal energy structure of the ion can have an impact on the degree of 2PSE enhancement achievable and find that divalent rare earths are more favorable.

DOI: 10.1103/PhysRevB.107.195420

I. INTRODUCTION

Two-photon spontaneous emission (2PSE) is a decay process whereby an electronic transition occurs via emission of a photon pair whose combined energy is equal to the difference between the excited and ground states [1]. Compared to single-transition decay, 2PSE usually occurs at a much lower rate, as it requires a transition to an intermediate state. In atomic systems these states are typically found at energies far from the initial and final states, and they are only weakly connected through an electric dipole perturbation. This leads to 2PSE decay rates that are commonly 10^8 lower than single-channel transition rates [2]. Despite this low efficiency, 2PSE has generated interest as a mechanism for the creation of entangled photon pairs that would be useful in quantum information systems [3]. In particular, the 2PSE process naturally generates photon pairs that are entangled polarization [4,5] and frequency states [6]. Moreover, the theoretical bounds on 2PSE permit it to, in principle, generate photon pairs at higher rate than state-of-the-art parametric down-conversion schemes and over a wider range of frequencies.

In order to enhance 2PSE to a level that is useful in real-world applications, multiple research efforts have investigated solid-state systems, including quantum wells [7] and quantum dots [8], that permit higher rates of 2PSE. In some experiments, the intermediate state is engineered to exist between the initial and final states, creating a resonant condition in the decay process that enhances the 2PSE transition rate. Other works have considered metallic nanostructures as a method of enhancing 2PSE by supporting plasmonic resonances [9]. More recently, it was theoretically predicted that two-dimensional (2D) materials that support highly confined optical modes, including surface plasmons in graphene [10,11] and surface polaritons in hexagonal boron nitride [12], could dramatically enhance 2PSE from nearby emitters through the Purcell effect. The underlying premise of those predictions is that the enhancement of single- and two-photon processes scale with the third and sixth powers, respectively, of the confinement factor of an optical mode [11]. In 2D materials, this confinement factor, which can be approximated as the ratio between the free-space and surface mode wavelengths, can be $\sim 10^2$, large enough to allow 2PSE rates to approach those of single-transition decay. Indeed, theoretical studies have shown that hydrogen atoms suspended above graphene [11], graphene nanodisks [10], and monolayer hexagonal boron nitride [12] can exhibit 2PSE rates that become comparable to or even exceed the corresponding single-transition decay processes. However, despite numerous predictions, there has been no experimental evidence of 2PSE occurring in graphene-coupled emitters, even though many works have studied such systems in detail [13–25]. Factors that make observations of 2PSE challenging include (1) the strong quenching effect of graphene on nearby emitters, driven by nonradiative energy transfer as well as coupling to nonradiative surface modes; (2) the high inefficiencies and low speeds of detectors in the mid- to far IR, where graphene-mediated 2PSE is likely to occur; and (3) the competing processes that drive emitter decay, which can also depend on doping and distance from graphene. Even with these barriers, however, a strongly enhanced 2PSE rate should perturb the overall observed lifetime of a graphene-coupled emitter, and such a perturbation has not been revealed in detailed lifetime measurements.

In this work we perform a comprehensive theoretical analysis of 2PSE from fluorescent rare earth atoms that are optically coupled to graphene and graphene nanoribbons. Our focus on rare earths reflects the fact that they can exhibit

*vbrar@wisc.edu

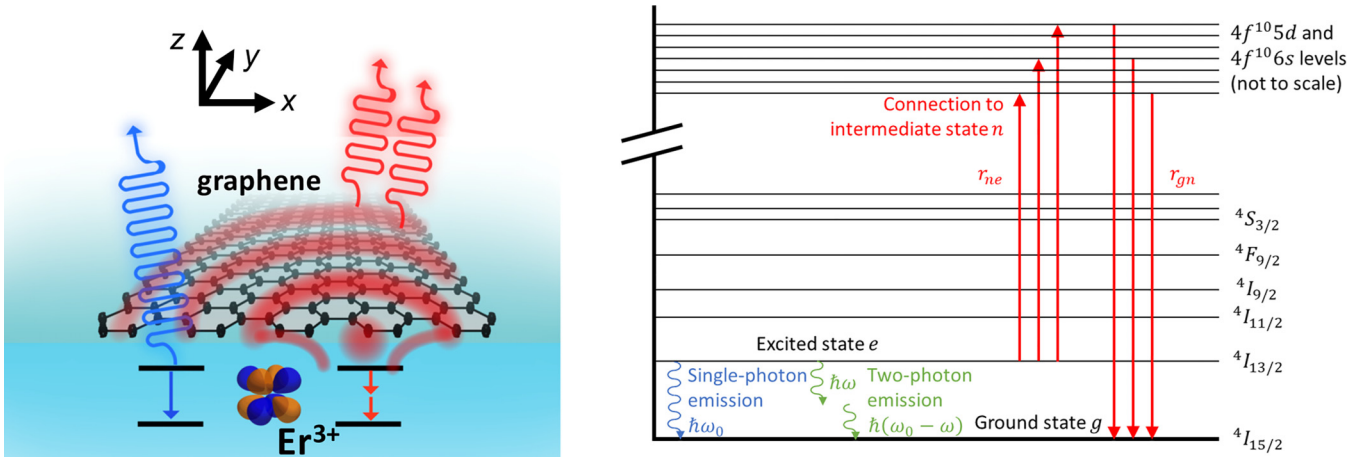

FIG. 1. Left: schematic of an emitter beneath a graphene nanoribbon, with single-transition decay shown in blue and 2PSE shown in red. Right: energy levels for the processes involved in two-photon spontaneous emission for Er^{3+}. An electron relaxes from the $^4I_{13/2}$ state to the $^4I_{15/2}$ state, but the matrix elements that determine the process's strength are defined by the electric dipole transitions to the higher $4f^{10}5d$ and $4f^{10}6s$ states.

high-efficiency emission at sufficiently long wavelengths to couple with graphene plasmonic modes which, for achievable carrier densities, are heavily damped at wavelengths < 1 μm. Infrared emissions from these ions occur between their $4f$ electron states, which are located close to the nucleus, causing the emission spectra to remain largely consistent across different host crystals [26]. For Er^{3+}, photonic crystal designs have been proven to be effective in enhancing emission sufficiently to observe fluorescence of individual ions [27]. Rare earth doped substrates can also be grown via ion implantation or molecular beam epitaxy, where the placement of dopants can be controlled with nanometer precision [28–31], and multiple experiments have shown that graphene can affect the emission properties of nearby rare earth ions [13,14]. Here we theoretically investigate both single-transition decay and 2PSE from rare earths near graphene as a number of parameters are varied, including emitter orientation, rare earth species, graphene nanostructure geometry, and graphene doping levels.

A basic illustration of our model system is shown in Fig. 1, where a rare earth atom—in this case trivalent erbium (Er^{3+})—is placed near a graphene sheet or nanoribbon. Upon excitation, the atom can decay nonradiatively or radiatively via single-transition decay or 2PSE, emitting photons and/or graphene surface plasmons in the process. All of these processes are affected by the graphene, which provides pathways for nonradiative and radiative decay that are dependent on the graphene carrier density and also on the graphene geometry. The refractive index of the material in which the emitter is located also has an effect on the emission rates, as do nearby material-air interfaces, which perturb the local optical density of states. Those changes are discussed in the Supplemental Material [32] (see also Refs. [33–37] therein), but they do not substantially affect our analysis below, which focuses only on the role of graphene.

In order to precisely quantify the graphene-rare-earth interaction, we first determine the relative rates of single-transition decay and 2PSE from the rare earth atoms by numerically calculating the transition probabilities between all intermediate states, which is detailed for Er^{3+} in Sec. II. In Sec. III we use full field finite difference time domain (FDTD) simulations to calculate the enhancement of both single-transition decay and 2PSE from Er^{3+} due to both radiative and nonradiative processes enabled by the presence of graphene. Next, in Sec. IV we explore how graphene affects the 2PSE in divalent samarium and thulium, which have energy levels that are more favorable to 2PSE in comparison to Er^{3+}. Finally, we discuss how our calculations compare to previous works and experimental configurations for which we predict graphene-enhanced 2PSE will be observable.

II. DETERMINATION OF 2PSE RATES IN RARE EARTHS

Contrary to single-photon emission, in which an ion transitions from an excited state $\hbar\omega_e$ to the ground state $\hbar\omega_g$ by emitting a single photon of energy $\hbar\omega_0 = \hbar(\omega_e - \omega_g)$, 2PSE allows the ion to emit two simultaneous photons, one of energy $\hbar\omega$ and the other of energy $\hbar(\omega_0 - \omega)$. As a second-order process, 2PSE requires a sum over all intermediate states $\hbar\omega_n$ that are connected to the initial and final states by electric dipole selection rules. The total 2PSE rate Γ_0 can be written in terms of the spectral 2PSE rate γ_0, which takes the form [38]

$$\begin{aligned}\Gamma_0 &= \int_0^{\omega_0} \gamma_0(\omega)d\omega \\ &= \frac{4c}{3\pi}\alpha^2 k^5 \int_0^1 y^3(1-y)^3 \left|\sum_n r_{gn} r_{ne} \right. \\ &\quad \left. \times \left(\frac{1}{(\omega_n-\omega_e)/\omega_0 + y} + \frac{1}{(\omega_n-\omega_e)/\omega_0 + 1 - y}\right)\right|^2 dy,\end{aligned} \tag{1}$$

where r_{gn} and r_{ne} represent the electric dipole matrix elements connecting the intermediate energy level to the ground state and excited state, respectively. The variable of integration y represents the fraction of the total emission energy accounted for by the first photon, with the second accounting for $1 - y$. A diagram of the intermediate transition processes involved

in 2PSE for Er^{3+} is shown in Fig. 1, along with the ${}^4I_{13/2} \rightarrow {}^4I_{15/2}$ transition for single-channel decay.

Although the ${}^4I_{13/2} \rightarrow {}^4I_{15/2}$ transition is the dominant emission process in Er^{3+} within a material host (e.g., Y_2O_3), it is classically electric dipole forbidden due to both states having the $4f^{11}$ configuration, which has odd parity. The strength of the transition arises from the mixing of these states with higher-lying even-parity states in the $4f^{10}5d$ and $4f^{10}6s$ configurations, which occurs due to the host crystal structure breaking the symmetry of the wave function [39,40]. Similarly, for 2PSE, the matrix elements r_{gn} and r_{ne} in Eq. (1) that connect the ${}^4I_{13/2}$ and ${}^4I_{15/2}$ states to other $4f^{11}$ states will be nonzero; however, the dominant contributions will originate from the electric dipole allowed even-parity ($4f^{10}$) states. To determine r_{gn} and r_{ne}, we use Cowan's atomic structure codes to calculate the wave functions, diagonalize the matrix, and calculate the resulting transition matrix elements [41]. This allows us to numerically calculate the energy levels for all $4f^{10}5d$ and $4f^{10}6s$ states along with the oscillator strengths for all electric dipole transitions between them and the ${}^4I_{13/2}$ and ${}^4I_{15/2}$ states. The energy levels for the $4f^{10}5d$ and $4f^{10}6s$ levels used for ω_n in Eq. (1) are adjusted from the outputs of Cowan's code by adding a constant amount to each, setting the lowest-energy dipole-allowed state to the published value of 73 458 cm^{-1} above the ground state [42]. Using these matrix elements in Eq. (1) and a single-photon emission frequency of $\omega_0 = 6500\ cm^{-1}$ [43], we compute a spontaneous two-photon emission rate for Er^{3+} of $\Gamma_0 = 2.943\times10^{-7}\ s^{-1}$. Comparing this value to the experimentally determined single-photon spontaneous emission rate of 125 s^{-1} for Er^{3+} in Y_2O_3 [44], we show that the two processes differ by more than eight orders of magnitude; this relative difference is comparable to what has been predicted for the $2s \rightarrow 1s$ two-photon transition in hydrogen compared to the $2p \rightarrow 1s$ single-photon transition [2].

III. ENHANCEMENT OF 2PSE AND SINGLE-TRANSITION DECAY IN Er^{3+} BY GRAPHENE AND GRAPHENE NANORIBBONS

While intrinsic 2PSE rates are substantially less than those of single-transition decay, it has been predicted that they can be made comparable by using Purcell enhancement, wherein the decay rate of an emitter is enhanced in the presence of confined optical modes [11]. This process can occur in any optical cavity, but it can be especially strong in graphene and other 2D materials, which support optical surface waves with wavelengths much shorter than free space. These modes, which include surface plasmons and phonon polaritons, enhance single-photon emission rates by a factor that scales with $\eta_0^3 = (\lambda_0/\lambda_p)^3$, where λ_0 is the free-space wavelength and λ_p is the wavelength of the surface mode. For two-photon processes, the enhancement scales as η_0^6. While metals can support surface modes with $\eta_0 \sim 10$, graphene plasmons exhibit $\eta_0 > 100$ [45], leading to substantially more 2PSE enhancement over single-transition decay processes. Moreover, when the graphene is patterned into a nanostructure that supports resonant plasmonic modes, the emission enhancement is further increased by the Q factor of the resonance, which can be made to selectively occur at specific frequencies, and the emitted plasmonic modes can more efficiently out-couple to free space. Such nanostructures can be fabricated with precise width control using bottom-up [46] and top-down [47] lithography methods, and theoretical works have shown the resulting plasmonic resonances depend only weakly on the graphene edge configuration for widths greater than 10 nm [48].

In general, the modification of the differential two-photon spontaneous emission rate in the presence of a surface is given by [49]

$$\frac{\gamma(\omega,\mathbf{r})}{\gamma_0(\omega)} = \frac{\sum_{i,j}|D_{ij}(\omega,\omega_0-\omega)|^2 P_i(\omega,\mathbf{r})P_j(\omega_0-\omega,\mathbf{r})}{\sum_{i',j'}|D_{i'j'}(\omega,\omega_0-\omega)|^2}. \tag{2}$$

Here $P_i(\omega,\mathbf{r})$ depends on the confinement factor η_0, the wave number k, and the surface-emitter distance z_0 according to $P_i(\omega,\mathbf{r}) \sim \eta_0^3 \exp(-2\eta_0 k z_0)$ [11] and represents the Purcell enhancement of an electric dipole at location $\mathbf{r}$ emitting at frequency ω and oriented along the axis $i = [x, y, z]$. The matrix D_{ij} depends on the electric dipole matrix elements $\mathbf{d}_{ne}$ and $\mathbf{d}_{gn}$ connecting the intermediate states n to the excited and ground states, respectively, and is given by

$$D(\omega_1,\omega_2) = \sum_n \left(\frac{\mathbf{d}_{ne}\mathbf{d}_{gn}}{\omega_n - \omega_e + \omega_1} + \frac{\mathbf{d}_{gn}\mathbf{d}_{ne}}{\omega_n - \omega_e + \omega_2} \right). \tag{3}$$

For a hydrogenic ion whose excited and ground configurations are both s orbitals, D_{ij} will be diagonal, as the dipole-allowed intermediate p states are aligned along a specific x, y, or z axis and can be reached only when both transitions have the same polarization. For more complicated ions such as Er^{3+}, however, the off-diagonal terms will, in general, not be zero, and their values may be computed by using the Wigner-Eckart theorem to calculate the irreducible tensor components for each transition [41,50,51]. After minor simplifications, we find that the off-diagonal components for Er^{3+} contribute 3/4 as strongly as the diagonal ones, so the differential 2PSE enhancement is given by

$$\frac{\gamma(\omega,\mathbf{r})}{\gamma_0(\omega)} \approx \sum_{i,j} A_{i,j} P_i(\omega,\mathbf{r}) P_j(\omega_0-\omega,\mathbf{r}), \tag{4}$$

with

$$A = \begin{pmatrix} 2/15 & 1/10 & 1/10 \\ 1/10 & 2/15 & 1/10 \\ 1/10 & 1/10 & 2/15 \end{pmatrix}. \tag{5}$$

Further details about this calculation can be found in the Supplemental Material [32].

Computational methods such as finite difference and finite element methods provide a tool that can be used to analyze the modification of emission rates in a variety of plasmonic environments [52]. To calculate the P_i factors in Eq. (4), we use FDTD (LUMERICAL) simulations to monitor the power emitted from an electric dipole source placed 5 nm below the graphene as a function of frequency and graphene Fermi level E_F. We consider the effects of both a continuous graphene sheet as well as ribbons designed in an array with a period equal to 3 times the ribbon width, with the dipole source positioned beneath the center of the ribbon. In all simulations, the graphene dielectric properties are modeled using a surface

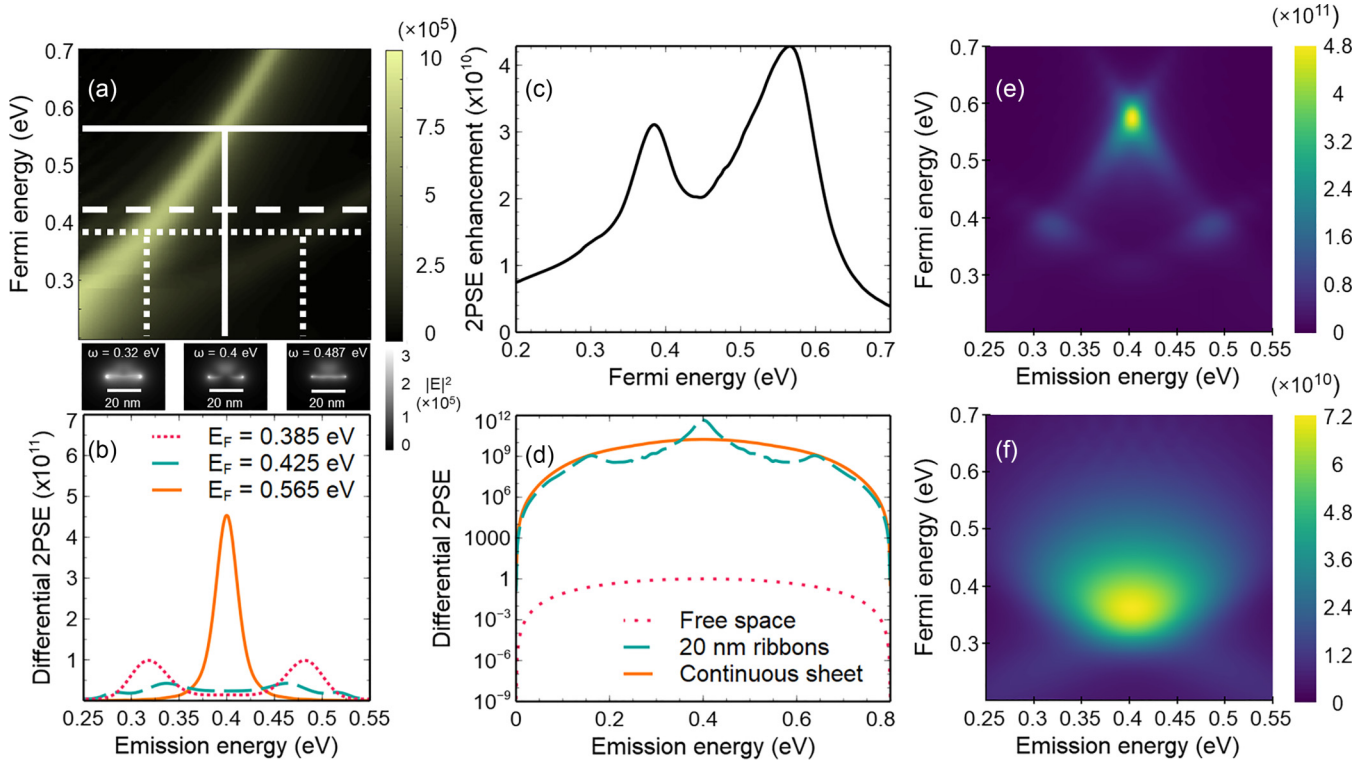

FIG. 2. Results for a single-dipole orientation. All results consider an Er^{3+} emitter 5 nm away from graphene structures, with the dipole moment oriented along the short dimension of the ribbons (or parallel to the sheet). (a) Purcell enhancement for the emitter near 20 nm graphene ribbons. Horizontal lines correspond to the Fermi energies plotted in (b), while vertical lines show the doubly resonant frequencies for photon emission. Electric field profiles at $E_F = 0.385$ eV are shown below, calculated at a lateral distance of 7 nm along the ribbon with the field strength normalized to the value with no graphene present. (b) Differential 2PSE enhancement $\gamma/\gamma_{0,\max}$ for the emitter near graphene ribbons for doubly resonant Fermi energies (pink dotted and orange solid lines) and a nonresonant Fermi energy (blue dashed line). (c) Integrated 2PSE enhancement Γ/Γ_0 for the emitter near 20 nm wide graphene ribbons. (d) Differential 2PSE enhancement $\gamma/\gamma_{0,\max}$ at $E_F = 0.565$ eV for the emitter with no graphene present (pink dotted line), modified by graphene ribbons (blue dashed line) and modified by a graphene sheet (orange solid line). Differential 2PSE enhancement $\gamma/\gamma_{0,\max}$ for the emitter near (e) graphene ribbons or (f) a graphene sheet. The results in (b), (d), (e), and (f) are normalized by the maximum value of free-space differential 2PSE.

conductivity formalism [53], which includes both interband and intraband terms. To account for roughness and charge disorder, the mobility is set to 500 $cm^2/V\,s$, a value consistent with graphene grown via chemical vapor deposition and fitted experimentally in previous measurements of graphene plasmons [47,54–57].

We note that interactions between an emitter and nearby graphene occur through three main mechanisms depending on the Fermi energy to which the graphene is tuned [13,14,58–62]. When the Fermi energy E_F is less than half the emitter energy, that energy is transferred to graphene by exciting an electron-hole pair. At higher values of E_F, the emitter instead transfers most of its energy to free space in the form of propagating photons, or it is damped by Ohmic loss in the graphene sheet. At still higher values of Fermi energy, when E_F exceeds ~70% of the emission energy, the emission couples to plasmonic modes supported by the graphene. All three can, in principle, contribute to the enhancement of the decay rate; however, the enhancement by plasmonic modes is orders of magnitude larger than the other interaction mechanisms, and when two photons or plasmons are considered, this difference is increased further, such that decay pathways via two-plasmon transitions dominate. We therefore identify the emission enhancement due to graphene as Purcell enhancement throughout this text, although other nonradiative pathways make minor contributions.

In Fig. 2(a), we plot $P_x(\omega, \mathbf{r})$ for the case of a dipole emitter placed 5 nm beneath a 20 nm wide graphene nanoribbon, with the dipole axis oriented along the short axis of the ribbon. The effects of placing the emitter beneath the gap or the ribbon's edge as well as changing the emitter's orientation or the ribbon's width are all discussed in the Supplemental Material [32]. For a given value of E_F, it is observed that $P_x(\omega, \mathbf{r})$ shows two maxima of magnitude 10^5–10^6, which correspond to the first- and second-order plasmonic resonances supported by the graphene nanoribbon, consistent with previous works [60].

For 2PSE, emission of one photon at frequency ω is accompanied by another at $\omega_0 - \omega$, and the total enhancement is determined by the factor $P_i(\omega, \mathbf{r}) \times P_j(\omega_0 - \omega, \mathbf{r})$. When both photons are matched to plasmonic resonances, the 2PSE shows strong enhancement at particular energies; conversely, when one or more photons are not matched to a plasmonic resonance, 2PSE is suppressed. This behavior is illustrated in Fig. 2(b), which shows that for $E_F = 0.565$ eV there is a strong enhancement of the differential 2PSE near 0.4 eV

(3.1 μm) due to the plasmonic resonance supported in the graphene nanoribbon at that energy, which simultaneously enhances the emission of both 2PSE photons. Likewise, when E_F is tuned to 0.385 eV, plasmonic resonances are supported in the nanoribbon at both 0.32 and 0.49 eV. These support simultaneous emission of photons at both energies which, combined, equal the overall transition energy. This process leads to correspondingly large differential 2PSE enhancements at those photon energies. For an E_F of 0.385 eV, however, the nanoribbons support resonances at 0.34 and 0.53 eV, and thus, each resonant emission must be accompanied by a nonresonant process with minimal enhancement, causing the differential 2PSE to be low at both energies. This behavior is further illustrated in Fig. 2(c), where the wavelength-integrated 2PSE enhancement is plotted as a function of E_F, showing maxima when the nanoribbons support plasmonic resonances at energies that can be summed or doubled to equal the overall Er^{3+} transition energy.

The localized resonances in graphene nanoribbons provide energy selectivity to the 2PSE process and also aid in free-space emission; however, their relatively low quality factors ($Q \sim 10$) make it such that they do not enhance 2PSE substantially above what is realized in unpatterned graphene, which supports highly confined plasmonic modes over a large bandwidth. This is illustrated in Figs. 2(d)–2(f), where the differential 2PSE enhancement is compared between bare graphene and graphene nanoribbons over a range of carrier densities. Both exhibit enhancements of 10^{10}–10^{11}, and while the differential enhancement at $\frac{1}{2}\omega_0 \sim 0.4$ eV can be greater for tuned nanoribbons than unpatterned graphene, the total 2PSE enhancement is comparable for both geometries.

The above analysis considers only emitters with dipole orientations along the x axis as defined in Fig. 1, which most effectively couple to the plasmonic resonances of the ribbon. Aligning the dipole along the y and z axes allows for emission into the unbound plasmonic resonances that propagate along the length of the ribbon and behave identically to the unpatterned graphene and into localized "dark" mode resonances that have no net dipole moment but can still couple to nearby emitters [60]. The overall enhancement factors for different dipole orientations do not vary significantly; however, the dark resonances do occur at different frequencies than the resonances observed for an x-polarized dipole (see the Supplemental Material [32]). As a result, when all dipole orientations are averaged together (including cross terms), the net effect of the nanoribbons is a Fermi-level-dependent 2PSE enhancement that has less well defined maxima but that reaches an enhancement of 4×10^{10} and 5×10^{10} for the nanoribbons and unpatterned graphene, respectively, as shown in Fig. 3(a). The lateral position of the emitter also affects the magnitude of the Purcell enhancement (see the Supplemental Material [32]). Emitters located in the middle of the gap between two ribbons experience approximately an order of magnitude less enhancement than those directly beneath the nanoribbons.

Although 2PSE is dramatically enhanced in both patterned and unpatterned graphene, the majority of the emission occurs in the form of confined plasmonic modes, which mostly decay nonradiatively. However, some fraction of the emitted plasmons weakly couples to free space as far-field photons.

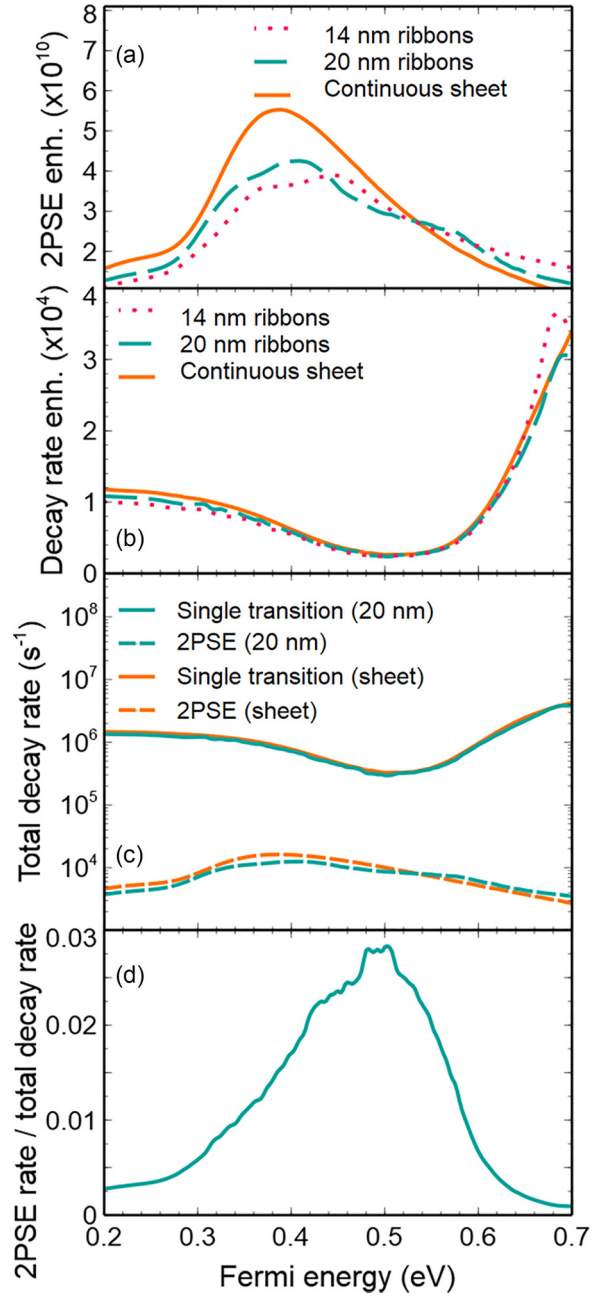

FIG. 3. Comparison of single-transition decay and two-photon emission. All results consider an Er^{3+} emitter 5 nm away from graphene structures, with all dipole orientations averaged according to Eq. (4). (a) Enhancement Γ/Γ_0 of total two-photon emission relative to a dipole with no graphene present. (b) Enhancement of single-transition decay at 1538 nm relative to a dipole with no graphene present. (c) Total single-transition decay rate compared to total two-photon emission rate in the presence of 20 nm ribbons and a continuous graphene sheet. (d) Fraction of total decay rate that can be attributed to 2PSE for 20 nm graphene ribbons.

In Fig. 4 we calculate the total, Fermi-energy-dependent, enhancement of 2PSE from Er^{3+} that results in far-field photon pairs due to continuous graphene and graphene nanoribbons. These results, which consider randomized dipole orientations, were performed by monitoring far-field radiation from

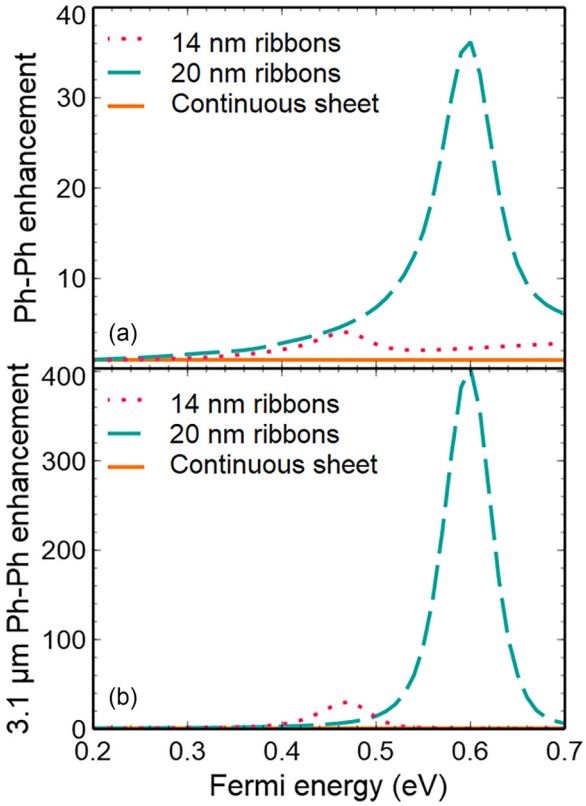

FIG. 4. Enhancement of two-photon emission. All results consider an Er^{3+} emitter 5 nm away from graphene structures, with all dipole orientations averaged according to Eq. (4). (a) Enhancement of purely radiative (photon-photon) emission. (b) Enhancement of purely radiative (photon-photon) emission in the 3–3.2 μm range.

a dipole with and without the presence of graphene. The resulting far-field enhancement factors were then utilized in place of the $P_i(\omega, r)$ factors in Eq. (4) to obtain the graphene nanoribbon enhancement of two-photon far-field emission. We find only modest enhancements, with the continuous graphene sheet providing no benefit and the graphene nanoribbon enhancement reaching ∼35. However, as shown in Fig. 4(b), the differential enhancement exceeds 400 when emitting near $\frac{1}{2}\omega_0 \sim 0.4$ eV (3.1 μm), where the emitted photon pairs have similar energies. Our calculations show that 20 nm wide nanoribbons display substantially more enhancement than 14 nm nanoribbons, despite the latter supporting larger confinement factors in the resonant modes at ∼0.4 eV (3.1 μm). We attribute this behavior to the better free-space photon-plasmon wavelength matching of the 20 nm nanoribbons. However, we note that even with enhancement factors of 400, the free-space 2PSE is still six orders smaller than conventional single-transition decay for Er^{3+}. The degree of free-space emission enhancement can reach $\sim 10^6$ when we instead consider emission in which one decay radiates to the far field and the other decays nonradiatively, creating a nonentangled, down-converted photon; this behavior is demonstrated in the Supplemental Material [32].

While we find the production of free-space photons to be inefficient via graphene-enhanced 2PSE, it is interesting to investigate how it affects the overall lifetime of Er^{3+}. In order to understand the relative contribution of the 2PSE, it is necessary to also calculate the enhancement by graphene of conventional single-transition decay for Er^{3+}, which is found by calculating the Fermi-level-dependent factor $P_i(\omega, \mathbf{r})$ at $\omega = 0.8$ eV with the dipole 5 nm from the graphene surface, averaged over all orientations. Figure 3(b) shows the results of those calculations for a continuous sheet of graphene, as well as nanoribbbons 14 and 20 nm wide, revealing enhancement factors of $\sim 10^4$, consistent with previously published predictions [60]. The total emission rates of both single-transition decay and 2PSE can be obtained by multiplying their respective enhancement factors by their free-space rates, which is shown in Fig. 3(c). These results show that while the 2PSE enhancement is six orders higher than single-transition enhancement for Er^{3+}, the overall 2PSE rate is still less than single-transition decay by more than a factor of 10. These results are due to the large difference in initial base rates between single-transition decay and 2PSE, which differ by more than 10^8. A similar result regarding 14 nm ribbons is shown in the Supplemental Material [32]. Finally, Fig. 3(d) shows the Fermi level-dependent fraction of 2PSE compared to the total decay rate of Er^{3+} modified by 20 nm graphene ribbons. It can be seen that the 2PSE can exceed 2.5% of the total decay at an optimal Fermi energy of $E_F \sim 0.5$ eV.

IV. ENHANCEMENT OF 2PSE IN Sm^{2+} AND Tm^{2+}

The low relative amounts of 2PSE achievable in Er^{3+} via graphene plasmon enhancement are due primarily to the low initial base rates of 2PSE, as well as the large amount of enhancement in competing single-transition decay processes. This motivates the search for other emitters in which one or both of those factors are mitigated. To this end, we investigate other rare earth ions that are potentially better suited for realization of a 2PSE-dominant emission source. In particular, one factor contributing to the low base 2PSE rates in Er^{3+} is the large energy spacing between the low-lying $4f^{11}$ states and the dipole-allowed $4f^{10}5d$ and $4f^{10}6s$ states. This causes the $\omega_n - \omega_e$ term in the denominator of Eq. (1) to be much larger than the single-photon emission frequency ω_0, reducing the overall 2PSE rate. In divalent rare earth ions, the intermediate states have much lower relative energies above the ground level when compared to their trivalent counterparts [63]. We consider two such divalent ions, Sm^{2+} and Tm^{2+}. Both of these ions have been synthesized and measured in photoluminescence experiments in fluorides as well as other compounds [64]. The first dipole-allowed excited states in these ions are at approximately 24 500 and 25 000 cm^{-1} relative to the ground state, which are lower than the corresponding Er^{3+} level by a factor of more than 2. Similar to Er^{3+}, these dipole-allowed states act as intermediate states for 2PSE and, through state mixing, enable lower-energy single-photon transitions that are classically electric dipole forbidden. Experimental measurements of Sm^{2+} ions in SrF_2 show single-photon emission at 14 350 cm^{-1} with a rate of 83.3 s^{-1} when temperature conditions are optimal (<45 K) [65]. For Tm^{2+} ions in CaF_2, the corresponding process occurs at 8966 cm^{-1} with a rate of 278 s^{-1} at liquid nitrogen temperatures [66]. Applying Eq. (1) to these ions, using oscillator strengths computed through Cowan's code and energy levels adjusted to match

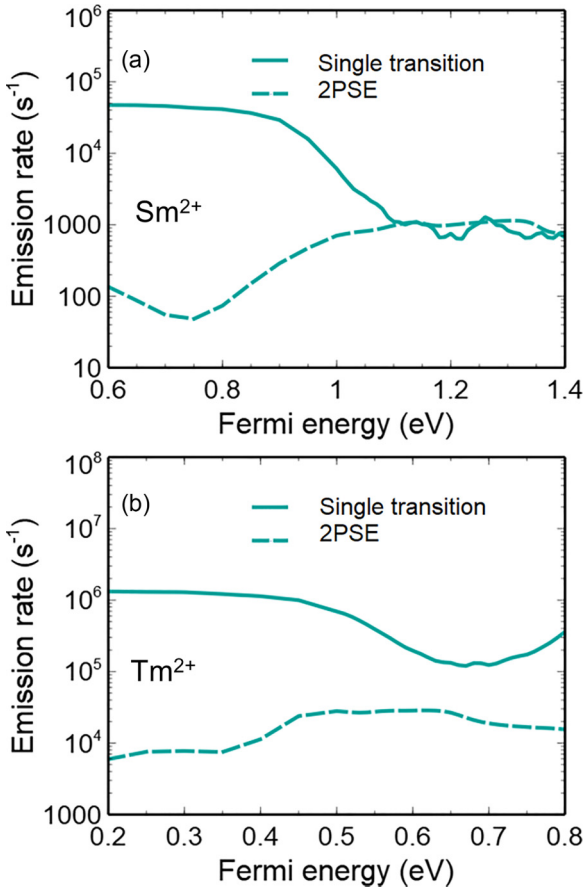

FIG. 5. Comparison of total single-transition decay and 2PSE rates for (a) Sm^{2+} and (b) Tm^{2+} when modified by 20 nm graphene ribbons. All results consider an emitter 5 nm away from graphene structures, with all dipole orientations averaged according to Eq. (4).

the experimentally measured first dipole-allowed level [67], we find the free-space 2PSE rates for Sm^{2+} and Tm^{2+} are 1.928×10^{-6} and 2.386×10^{-6} s^{-1}, respectively. These base rates for Sm^{2+} and Tm^{2+} are closer to the experimentally measured single-transition decay rates by factors of 9.8 and 3.6, respectively, in comparison to Er^{3+}.

Next, we explore the relative enhancements by graphene plasmons of 2PSE and single-transition decay in Sm^{2+} and Tm^{2+} using the same methodology described in Sec. III. Both the single-transition decay and 2PSE rates for the divalent emitters 5 nm beneath 20 nm graphene ribbons are shown in Fig. 5, computed here using theoretical single-photon emission frequencies of 15 223 cm^{-1} (1.89 eV) for Sm^{2+} and 8421 cm^{-1} (1.04 eV) for Tm^{2+} [41]. These results show that for Sm^{2+}, the 2PSE rate can equal the single-transition decay rate, while for Tm^{2+} the 2PSE rate is able to reach nearly 20% of the single-transition rate. The equivalence of the two rates for Sm^{2+} is expected to occur in only a limited window, as the single-transition rate will increase at larger values of E_F due to intraband transitions [13], which is observed in both Er^{3+} and Tm^{2+}. Both divalent ions, however, require high Fermi levels to achieve a maximal 2PSE fraction. For Tm^{2+}, the optimal Fermi energy of 0.65 eV is beyond what is achievable via electrostatic gating but can be reached with ionic liquid gating schemes [13,46,68]; for Sm^{2+}, however, Fermi energies exceeding 1.1 eV are required, which is potentially realizable using chemical doping techniques [69,70].

V. DISCUSSION

Our calculations predict 2PSE rates via graphene plasmon enhancement that are significantly lower than previously published results, which predicted that 2PSE could easily exceed single-transition decay rates when enhanced with surface modes in 2D materials [10–12]. There are two primary reasons for this difference. First, previous works studied emitter systems with large transition moment lengths ($\mathbf{d} = \langle f|\mathbf{x}|i\rangle$), such as the $4s \rightarrow 3s$ transition of hydrogen. Using the $5p$ state as the intermediate and incorporating all three dipole polarizations, the hydrogen $4s \rightarrow 3s$ transition has an average transition moment length of ∼2.3 Å between the two transitions that occur. Such systems have intrinsically large 2PSE base rates since the 2PSE rate approximately scales as $\mathbf{d}^4$ [12]. For the $4s \rightarrow 3s$ transition, for example, the 2PSE base rate is $\sim10^{-2}\,s^{-1}$. However, coupling an isolated hydrogen atom to a graphene surface that is a few nanometers away is experimentally challenging. In contrast, fluorescent solid-state "color centers" such as those we study here, which have larger atomic numbers, have substantially smaller dipole lengths, leading to lower overall 2PSE base rates; for Er^{3+}, each intermediate has an average transition moment length of around 0.4 Å or lower, and as shown in Sec. II, this emitter has a 2PSE base rate of $2.943\times10^{-7}\,s^{-1}$. Thus, while it is experimentally easier to couple graphene to solid-state emitters, the 2PSE enhancement must be much larger in order to be comparable to competing single-transition processes. Second, our calculations use a graphene model that considers a carrier mobility of 500 $cm^2/V\,s$, which is consistent with what is typical for graphene samples grown via chemical vapor deposition and placed on oxide surfaces [47,54–57] but is lower than mobilities considered in previous theoretical works, which assumed mobilities of 10 000 $cm^2/V\,s$ [10]. The effect of the lower mobility is to increase the single-channel decay rate enhancement [60] and, for the graphene nanoribbons, to decrease the 2PSE enhancement. This leads to a smaller fraction of ions exhibiting 2PSE in comparison to single-channel processes. A comparison of calculations performed using different mobilities is included in the Supplemental Material [32].

Thus, a main conclusion of this work is that when achievable material systems are considered, the prospects of realizing 2PSE as a dominant emission process are reduced. However, our calculations also indicate the conditions where the effects of 2PSE may be observable in experimentally testable systems. For example, rare earth doped substrates prepared via ion implantation or molecular beam epitaxy can be engineered to place ions at a fixed distance from an overlying graphene sheet. Lifetime-dependent emission measurements of such sample geometries have confirmed modification of the overall single-transition rate of Er^{3+} by both interband and intraband processes in graphene [13,14]. Our calculations indicate that similar experiments can be used to search for evidence of 2PSE by probing the Fermi-energy-dependent lifetime of Er^{3+} at 1538 nm, which should be affected by 2PSE near $E_F \sim 0.5$ eV, as shown in Fig. 3(d). The presence

of such a 2PSE contribution to overall decay rates would require lifetime measurements with a time resolution of ∼1 ns. Moreover, it is critical in such measurements that Er^{3+} has a highly uniform distance distribution from the graphene. Previous results were performed using experimental configurations with ∼1 μs time resolution, ∼1 μm spot size, and a broad distribution of distances such that the signal was dominated by ions located farther from the graphene, which are more likely to emit radiatively than through a plasmonic surface mode [13,14]. We note that such measurements would also be aided by measuring high-mobility samples, in which the substrate is treated or engineered to minimize charge disorder. Larger mobilities would suppress the enhancement of single-transition processes and allow 2PSE to play a larger relative role, making detection easier.

Direct detection of photons emitted from rare earth ions via 2PSE is also possible; however, only a small fraction ($\sim 10^{-9}$) of plasmon pairs generated via 2PSE are emitted to free space as photon pairs. In the limit of high excitation rates, the number of emitted photon pairs in the 3–3.2 μm wavelength range can be estimated to be 222 photon pairs per second. This assumes a Y_2O_3 substrate with a doped plane of 0.2% Er^{3+} that is 5 nm below an array of 20 nm graphene nanoribbons with $E_F = 0.6$ eV and with collection over a 10×10 μm^2 area. These numbers can be improved by using larger dopant concentrations and collection areas and larger graphene nanoribbons which have lower Purcell enhancements but more effectively couple plasmonic modes to free space. However, when emitters that are placed at random lateral positions relative to the graphene nanoribbons are considered, the overall 2PSE will be reduced.

Another possible route to verify our theoretical results is by probing two-photon absorption, the inverse process to 2PSE. In a two-photon absorption (2PA) measurement, two photons with frequencies summing to ω_0 are incident on an atomic system simultaneously, elevating an electron to a higher energy level from which it can decay [71]. The efficiency of this process is also dependent on $P_i(\omega, \mathbf{r}) \times P_j(\omega_0 - \omega, \mathbf{r})$, which, for single-frequency excitation, must satisfy the condition $\omega = \omega_0/2$. Thus, the large Purcell enhancements supported by graphene will also drive large 2PA, which can be monitored by measuring fluorescence at ω_0. For graphene systems coupled to rare earth ions, performing 2PA measurements on nanoribbons or some other patterned nanostructure would be required, as the plasmonic modes in a continuous sheet would not couple to free-space excitation.

Our calculations also point to the importance of utilizing emitters with large initial 2PSE base rates for experiments whose goal is to boost 2PSE via Purcell enhancement to a significant fraction of overall emission. While previous works showed that atomic hydrogen can achieve this condition, the experimental viability of such an approach is low. Nevertheless, other emitter systems could be considered, including fluorescent dyes, such as ruthenium complexes and rhodamine 123, and fluorescent biomolecules, such as green fluorescent protein chromophore. These emitters are expected to have transition dipole moments corresponding to lengths of 1.1–1.3 Å [72], 1.7 Å [73], and 1.4 Å [74], respectively. Alternatively, our results show that a detailed consideration of the intermediate energy levels allows for identification of emitters with larger 2PSE base rates. Specifically, we find that emitters with intermediate energy levels that are near the excited state, such as divalent rare earths, have larger 2PSE rates which, via Purcell enhancement, can approach single-transition rates.

VI. CONCLUSION

We have calculated the 2PSE base rates for Er^{3+}, Sm^{2+}, and Tm^{2+} and, using full field simulations, determined the degree to which Purcell enhancement from nearby graphene and graphene nanoribbons can enhance overall 2PSE. We showed that the overall 2PSE rate enhancement of Er^{3+} ions can exceed 4×10^{10} and that it is strongly dependent on the graphene Fermi level. Moreover, we showed that the production of entangled free-space photon pairs near 3.1 μm via 2PSE can be enhanced by 400 by graphene nanoribbons. In contrast to previous studies of hydrogen, we found that the 2PSE rate for Er^{3+} does not become a significant fraction of the overall decay, and we attributed this discrepancy to the low initial 2PSE base rate for Er^{3+} and the lower graphene mobility used in our calculations. These two factors, however, represent realistic experimental conditions, and we outlined ways in which 2PSE could be observed in Er^{3+}-doped substrates coated with graphene; such systems have already been explored experimentally in regimes where single-transition processes are affected by graphene. Finally, we found that controlling the emitter species can affect the 2PSE contribution to overall emission. Specifically, we showed that divalent rare earths that have intermediate states close in energy to the initial excited state have higher overall base rates of 2PSE, and we found that for Sm^{2+} and Tm^{2+}, Purcell enhancement can be used to make 2PSE a large overall fraction of the decay.

These findings provide specific guidance for future experiments that aim to generate photon pairs via 2PSE using Purcell enhancement. Moreover, they can be used to engineer next-generation devices that produce entangled photons at high rates for quantum information science applications.

ACKNOWLEDGMENTS

This material is based upon work supported by the U.S. Department of Energy Office of Science National Quantum Information Science Research Centers as part of the Q-NEXT center, which supported the work performed by C.W. and V.W.B. G.H. was supported by a Defense Advanced Research Projects Agency Young Faculty Award (Grant No. YFA D18AP00043). D.D.Y. was supported by the Vilas Associates Award of the University of Wisconsin–Madison.

[1] M. Göppert-Mayer, Über Elementarakte mit zwei Quantensprüngen, Ann. Phys. (Berlin, Ger.) **401**, 273 (1931).

[2] G. Breit and E. Teller, Metastability of hydrogen and helium levels, Astrophys. J. **91**, 215 (1940).

[3] A. Hayat, P. Ginzburg, and M. Orenstein, High-rate entanglement source via two-photon emission from semiconductor quantum wells, Phys. Rev. B **76**, 035339 (2007).

[4] W. Perrie, A. J. Duncan, H. J. Beyer, and H. Kleinpoppen, Polarization Correlation of the Two Photons Emitted by Metastable Atomic Deuterium: A Test of Bell's Inequality, Phys. Rev. Lett. **54**, 1790 (1985).

[5] T. Radtke, A. Surzhykov, and S. Fritzsche, Photon pairs with tailor-made entanglement obtained from the two-photon decay of atomic hydrogen, Phys. Rev. A **77**, 022507 (2008).

[6] A. Hayat, P. Ginzburg, D. Neiman, S. Rosenblum, and M. Orenstein, Hyperentanglement source by intersubband two-photon emission from semiconductor quantum wells, Opt. Lett. **33**, 1168 (2008).

[7] A. Hayat, P. Ginzburg, and M. Orenstein, Observation of two-photon emission from semiconductors, Nat. Photon. **2**, 238 (2008).

[8] Y. Ota, S. Iwamoto, N. Kumagai, and Y. Arakawa, Spontaneous Two-Photon Emission from a Single Quantum Dot, Phys. Rev. Lett. **107**, 233602 (2011).

[9] A. N. Poddubny, P. Ginzburg, P. A. Belov, A. V. Zayats, and Y. S. Kivshar, Tailoring and enhancing spontaneous two-photon emission using resonant plasmonic nanostructures, Phys. Rev. A **86**, 033826 (2012).

[10] Y. Muniz, A. Manjavacas, C. Farina, D. A. R. Dalvit, and W. J. M. Kort-Kamp, Two-Photon Spontaneous Emission in Atomically Thin Plasmonic Nanostructures, Phys. Rev. Lett. **125**, 033601 (2020).

[11] N. Rivera, I. Kaminer, B. Zhen, J. D. Joannopoulos, and M. Soljačić, Shrinking light to allow forbidden transitions on the atomic scale, Science **353**, 263 (2016).

[12] N. Rivera, G. Rosolen, J. D. Joannopoulos, I. Kaminer, and M. Soljačić, Making two-photon processes dominate one-photon processes using mid-IR phonon polaritons, Proc. Natl. Acad. Sci. USA **114**, 13607 (2017).

[13] K. J. Tielrooij, L. Orona, A. Ferrier, M. Badioli, G. Navickaite, S. Coop, S. Nanot, B. Kalinic, T. Cesca, L. Gaudreau, Q. Ma, A. Centeno, A. Pesquera, A. Zurutuza, H. de Riedmatten, P. Goldner, F. J. García de Abajo, P. Jarillo-Herrero, and F. H. L. Koppens, Electrical control of optical emitter relaxation pathways enabled by graphene, Nat. Phys. **11**, 281 (2015).

[14] D. Cano, A. Ferrier, K. Soundarapandian, A. Reserbat-Plantey, M. Scarafagio, A. Tallaire, A. Seyeux, P. Marcus, H. de Riedmatten, P. Goldner, F. H. L. Koppens, and K.-J. Tielrooij, Fast electrical modulation of strong near-field interactions between erbium emitters and graphene, Nat. Commun. **11**, 4094 (2020).

[15] T. N. Lin, L. T. Huang, G. W. Shu, C. T. Yuan, J. L. Shen, C. A. J. Lin, W. H. Chang, C. H. Chiu, D. W. Lin, C. C. Lin, and H. C. Kuo, Distance dependence of energy transfer from InGaN quantum wells to graphene oxide, Opt. Lett. **38**, 2897 (2013).

[16] F. Federspiel, G. Froehlicher, M. Nasilowski, S. Pedetti, A. Mahmood, B. Doudin, S. Park, J.-O Lee, D. Halley, B. Dubertret, P. Gilliot, and S. Berciaud, Distance dependence of the energy transfer rate from a single semiconductor nanostructure to graphene, Nano Lett. **15**, 1252 (2015).

[17] Z. Chen, S. Berciaud, C. Nuckolls, T. F. Heinz, and L. E. Brus, Energy transfer from individual semiconductor nanocrystals to graphene, ACS Nano **4**, 2964 (2010).

[18] A. Yeltik, G. Kucukayan-Dogu, B. Guzelturk, S. Fardindoost, Y. Kelestemur, and H. V. Demir, Evidence for nonradiative energy transfer in graphene-oxide-based hybrid structures, J. Phys. Chem. C **117**, 25298 (2013).

[19] E. Treossi, M. Melucci, A. Liscio, M. Gazzano, P. Samorì, and V. Palermo, High-contrast visualization of graphene oxide on dye-sensitized glass, quartz, and silicon by fluorescence quenching, J. Am. Chem. Soc. **131**, 15576 (2009).

[20] B. Guzelturk and H. V. Demir, Near-field energy transfer using nanoemitters for optoelectronics, Adv. Funct. Mater. **26**, 8158 (2016).

[21] J. Tisler, T. Oeckinghaus, R. J. Stöhr, R. Kolesov, R. Reuter, F. Reinhard, and J. Wrachtrup, Single defect center scanning near-field optical microscopy on graphene, Nano Lett. **13**, 3152 (2013).

[22] R. J. Stöhr, R. Kolesov, K. Xia, R. Reuter, J. Meijer, G. Logvenov, and J. Wrachtrup, Super-resolution fluorescence quenching microscopy of graphene, ACS Nano **6**, 9175 (2012).

[23] Y.-J. Yu, K. S. Kim, J. Nam, S. R. Kwon, H. Byun, K. Lee, J.-H. Ryou, R. D. Dupuis, J. Kim, G. Ahn, S. Ryu, M.-Y. Ryu, and J. S. Kim, Temperature-dependent resonance energy transfer from semiconductor quantum wells to graphene, Nano Lett. **15**, 896 (2015).

[24] L. Gaudreau, K. J. Tielrooij, G. E. D. K. Prawiroatmodjo, J. Osmond, F. J. García de Abajo, and F. H. L. Koppens, Universal distance-scaling of nonradiative energy transfer to graphene, Nano Lett. **13**, 2030 (2013).

[25] J. Kim, L. J. Cote, F. Kim, and J. Huang, Visualizing graphene based sheets by fluorescence quenching microscopy, J. Am. Chem. Soc. **132**, 260 (2010).

[26] G. Liu and B. Jacquier, *Spectroscopic Properties of Rare Earths in Optical Materials* (Springer, New York, 2005).

[27] A. M. Dibos, M. Raha, C. M. Phenicie, and J. D. Thompson, Atomic Source of Single Photons in the Telecom Band, Phys. Rev. Lett. **120**, 243601 (2018).

[28] A. M. Dibos, M. T. Solomon, S. E. Sullivan, M. K. Singh, K. E. Sautter, C. P. Horn, G. D. Grant, Y. Lin, J. Wen, F. J. Heremans, S. Guha, and D. D. Awschalom, Purcell enhancement of erbium ions in TiO_2 on silicon nanocavities, Nano Lett. **22**, 6530 (2022).

[29] M. K. Singh, G. Wolfowicz, J. Wen, S. E. Sullivan, A. Prakash, D. D. Awschalom, and F. J. Heremans, Development of a scalable quantum memory platform–Materials science of erbium-doped TiO_2 thin films on silicon, arXiv:2202.05376.

[30] M. Scarafagio, A. Tallaire, K.-J. Tielrooij, D. Cano, A. Grishin, M.-H. Chavanne, F. H. L. Koppens, A. Ringuedé, M. Cassir, D. Serrano, P. Goldner, and A. Ferrier, Ultrathin Eu- and Er-doped Y_2O_3 films with optimized optical properties for quantum technologies, J. Phys. Chem. C **123**, 13354 (2019).

[31] T. Zhong and P. Goldner, Emerging rare-earth doped material platforms for quantum nanophotonics, Nanophotonics **8**, 2003 (2019).

[32] See Supplemental Material at http://link.aps.org/supplemental/10.1103/PhysRevB.107.195420 for a derivation of the dipole transition matrix elements; variation of Purcell enhancement with dipole position, dipole orientation, and graphene nanoribbon width; emission of mixed radiative-nonradiative modes; the effect of the refractive index on the dipole emission rate; variation of the total decay rate with graphene nanoribbon width;

and variation of 2PSE and the single-transition decay rate with graphene mobility.

[33] D. Toptygin, Effects of the solvent refractive index and its dispersion on the radiative decay rate and extinction coefficient of a fluorescent solute, J. Fluoresc. **13**, 201 (2003).

[34] H. Khosravi and R. Loudon, Vacuum field fluctuations and spontaneous emission in the vicinity of a dielectric surface, Proc. R. Soc. London, Ser. A **433**, 337 (1991).

[35] E. Snoeks, A. Lagendijk, and A. Polman, Measuring and Modifying the Spontaneous Emission Rate of Erbium near an Interface, Phys. Rev. Lett. **74**, 2459 (1995).

[36] M. J. A. de Dood, J. Knoester, A. Tip, and A. Polman, Förster transfer and the local optical density of states in erbium-doped silica, Phys. Rev. B **71**, 115102 (2005).

[37] Y. Nigara, Measurement of the optical constants of yttrium oxide, Jpn. J. Appl. Phys. **7**, 404 (1968).

[38] D. P. Craig and T. Thirunamachandran, *Molecular Quantum Electrodynamics: An Introduction to Radiation-Molecule Interactions* (Academic Press, London, 1984).

[39] B. R. Judd, Optical absorption intensities of rare-earth ions, Phys. Rev. **127**, 750 (1962).

[40] G. S. Ofelt, Intensities of crystal spectra of rare-earth ions, J. Chem. Phys. **37**, 511 (1962).

[41] R. D. Cowan, *The Theory of Atomic Structure and Spectra* (University of California Press, Berkeley, 1981).

[42] A. Meftah, S. A. Mammar, J.-F. Wyart, W.-Ü. L. Tchang-Brillet, N. Champion, C. Blaess, D. Deghiche, and O. Lamrous, Analysis of the free ion spectrum of Er^{3+} (Er IV), J. Phys. B **49**, 165002 (2016).

[43] D. K. Sardar, K. L. Nash, R. M. Yow, and J. B. Gruber, Absorption intensities and emission cross section of intermanifold transition of Er^{3+} in Er^{3+}:Y_2O_3 nanocrystals, J. Appl. Phys. **101**, 113115 (2007).

[44] M. J. Weber, Radiative and multiphonon relaxation of rare-earth ions in Y_2O_3, Phys. Rev. **171**, 283 (1968).

[45] M. Jablan, H. Buljan, and M. Soljačić, Plasmonics in graphene at infrared frequencies, Phys. Rev. B **80**, 245435 (2009).

[46] J. F. Siegel, J. H. Dwyer, A. Suresh, N. S. Safron, M. A. Fortman, C. Wan, J. W. Choi, W. Wei, V. Saraswat, W. Behn, M. A. Kats, M. S. Arnold, P. Gopalan, and V. W. Brar, Using bottom-up lithography and optical nonlocality to create short-wave infrared plasmonic resonances in graphene, ACS Photon. **8**, 1277 (2021).

[47] V. W. Brar, M. S. Jang, M. Sherrott, J. J. Lopez, and H. A. Atwater, Highly confined tunable mid-infrared plasmonics in graphene nanoresonators, Nano Lett. **13**, 2541 (2013).

[48] S. Thongrattanasiri, A. Manjavacas, and F. J. García de Abajo, Quantum finite-size effects in graphene plasmons, ACS Nano **6**, 1766 (2012).

[49] Y. Muniz, F. S. S. da Rosa, C. Farina, D. Szilard, and W. J. M. Kort-Kamp, Quantum two-photon emission in a photonic cavity, Phys. Rev. A **100**, 023818 (2019).

[50] C. Eckart, The application of group theory to the quantum dynamics of monatomic systems, Rev. Mod. Phys. **2**, 305 (1930).

[51] E. Wigner, Einige Folgerungen aus der Schrödingerschen Theorie für die Termstrukturen, Z. Phys. **43**, 624 (1927).

[52] G. M. Akselrod, C. Argyropoulos, T. B. Hoang, C. Ciracì, C. Fang, J. Huang, D. R. Smith, and M. H. Mikkelsen, Probing the mechanisms of large Purcell enhancement in plasmonic nanoantennas, Nat. Photon. **8**, 835 (2014).

[53] G. W. Hanson, Dyadic Green's functions and guided surface waves for a surface conductivity model of graphene, J. Appl. Phys. **103**, 064302 (2008).

[54] M. S. Jang, V. W. Brar, M. C. Sherrott, J. J. Lopez, L. Kim, S. Kim, M. Choi, and H. A. Atwater, Tunable large resonant absorption in a midinfrared graphene Salisbury screen, Phys. Rev. B **90**, 165409 (2014).

[55] S. Kim, M. S. Jang, V. W. Brar, K. W. Mauser, L. Kim, and H. A. Atwater, Electronically tunable perfect absorption in graphene, Nano Lett. **18**, 971 (2018).

[56] T. Kobayashi, M. Bando, N. Kimura, K. Shimizu, K. Kadono, N. Umezu, K. Miyahara, S. Hayazaki, S. Nagai, Y. Mizuguchi, Y. Murakami, and D. Hobara, Production of a 100-m-long high-quality graphene transparent conductive film by roll-to-roll chemical vapor deposition and transfer process, Appl. Phys. Lett. **102**, 023112 (2013).

[57] A. Pirkle, J. Chan, A. Venugopal, D. Hinojos, C. W. Magnuson, S. McDonnell, L. Colombo, E. M. Vogel, R. S. Ruoff, and R. M. Wallace, The effect of chemical residues on the physical and electrical properties of chemical vapor deposited graphene transferred to SiO_2, Appl. Phys. Lett. **99**, 122108 (2011).

[58] J. D. Cox, M. R. Singh, G. Gumbs, M. A. Anton, and F. Carreno, Dipole-dipole interaction between a quantum dot and a graphene nanodisk, Phys. Rev. B **86**, 125452 (2012).

[59] V. D. Karanikolas, C. A. Marocico, and A. L. Bradley, Dynamical tuning of energy transfer efficiency on a graphene monolayer, Phys. Rev. B **91**, 125422 (2015).

[60] F. H. L. Koppens, D. E. Chang, and F. J. García de Abajo, Graphene plasmonics: A platform for strong light-matter interactions, Nano Lett. **11**, 3370 (2011).

[61] S.-A. Biehs and G. S. Agarwal, Large enhancement of Förster resonance energy transfer on graphene platforms, Appl. Phys. Lett. **103**, 243112 (2013).

[62] A. Manjavacas, S. Thongrattanasiri, D. E. Chang, and F. J. García de Abajo, Temporal quantum control with graphene, New J. Phys. **14**, 123020 (2012).

[63] P. Dorenbos, f → d transition energies of divalent lanthanides in inorganic compounds, J. Phys.: Condens. Matter **15**, 575 (2003).

[64] M. Suta and C. Wickleder, Synthesis, spectroscopic properties and applications of divalent lanthanides apart from Eu^{2+}, J. Lumin. **210**, 210 (2019).

[65] A. S. M. M. Alam and B. Di Bartolo, Thermal dependence of fluorescence and lifetimes of Sm^{2+} in several host lattices, J. Chem. Phys. **47**, 3790 (1967).

[66] Z. J. Kiss, Energy levels of divalent thulium in CaF_2, Phys. Rev. **127**, 718 (1962).

[67] W. C. Martin, R. Zalubas, and L. Hagan, *Atomic Energy Levels: The Rare-Earth Elements*, NBS Circular (US Government Printing Office, Washington, DC, 1978).

[68] Z. Fang, Y. Wang, A. E. Schlather, Z. Liu, P. M. Ajayan, F. J. García de Abajo, P. Nordlander, X. Zhu, and N. J. Halas, Active tunable absorption enhancement with graphene nanodisk arrays, Nano Lett. **14**, 299 (2014).

[69] I. Khrapach, F. Withers, T. H. Bointon, D. K. Polyushkin, W. L. Barnes, S. Russo, and M. F. Craciun, Novel highly conductive and transparent graphene-based conductors, Adv. Mater. **24**, 2844 (2012).

[70] Y. Song, W. Fang, A. L. Hsu, and J. Kong, Iron (III) chloride doping of CVD graphene, Nanotechnology **25**, 395701 (2014).

[71] Z. Lin and J. Vučković, Enhanced two-photon processes in single quantum dots inside photonic crystal nanocavities, Phys. Rev. B **81**, 035301 (2010).

[72] C. W. Stark, A. Trummal, M. Uudsemaa, J. Pahapill, M. Rammo, K. Petritsenko, M.-M. Sildoja, and A. Rebane, Solute-solvent electronic interaction is responsible for initial charge separation in ruthenium complexes $[Ru(bpy)_3]^{2+}$ and $[Ru(phen)_3]^{2+}$, Commun. Chem. **2**, 108 (2019).

[73] P.-H. Chung, C. Tregidgo, and K. Suhling, Determining a fluorophore's transition dipole moment from fluorescence lifetime measurements in solvents of varying refractive index, Methods Appl. Fluoresc. **4**, 045001 (2016).

[74] G. Bublitz, B. A. King, and S. G. Boxer, Electronic structure of the chromophore in green fluorescent protein (GFP), J. Am. Chem. Soc. **120**, 9370 (1998).